Unveiling the High-valence Oxygen Degradation Across the Delithiated Cathode Surface

Qinghao Li [a, b†], Qi Liang[a†], Hui Zhang[c], Sichen Jiao[b], Zengqing Zhuo[d], Junyang Wang[b], Qiang Li*[a], Jie-Nan Zhang*[b‡], Xiqian Yu*[b]

[a] Prof. Q-H. Li, Q. Liang, Prof. Q. Li,
College of Physics, Center for Marine Observation and Communications, Qingdao University,
Qingdao 266071, China
E-mail: liqiang@qdu.edu.cn,
[b] S. Jiao, Dr. J. Wang, Prof. J-N Zhang, Prof. X. Yu
Key Laboratory for Renewable Energy, Beijing Key Laboratory for New Energy Materials and Devices, Institute of Physics, Chinese Academy of Sciences,
Beijing 100190, China
E-mail: jnzhang@iphy.ac.cn, xyu@iphy.ac.cn,
[c] Dr. H. Zhang
State Key Laboratory of Functional Materials for Informatics, Shanghai Institute of Microsystem and Information Technology, Chinese Academy of Sciences,
Shanghai 200050, China
[d] Dr. Z. Zhuo
Advanced Light Source, Lawrence Berkeley National Laboratory, Berkeley, CA 94720, USA.
† These authors contributed equally to this work
‡ Current affiliation: National Natural Science Foundation of China (NSFC)

Supporting information for this article is given via a link at the end of the document.

Charge compensation on anionic redox reaction (ARR) has been promising to realize extra capacity beyond transition metal redox in battery cathodes. The practical development of ARR capacity has been hindered by high-valence oxygen instability, particularly at cathode surfaces. However, the direct probe of surface oxygen behavior has been challenging. Here, the electronic states of surface oxygen are investigated by combining mapping of resonant Auger electronic spectroscopy (mRAS) and ambient pressure X-ray photoelectron spectroscopy (APXPS) on a model $LiCoO_2$ cathode. The mRAS verified that no high-valence oxygen can sustain at cathode surfaces, while APXPS proves that cathode electrolyte interphase (CEI) layer evolves and oxidizes upon oxygen gas contact. This work provides valuable insights into the high-valence oxygen degradation mode across the interface. Oxygen stabilization from surface architecture is proven a prerequisite to the practical development of ARR active cathodes.

The pursuit of alkali metal ion batteries with high energy density has been the key to the modern renewable energy industry, where designing and developing high-capacity cathode materials are deemed a critical part. Traditional cathodes rely on the transition metal (TM) redox to realize charge compensation during cycles, which is approaching its theoretical capacity limit. In the past decade, anionic redox reaction (ARR) has emerged as a promising scheme to support extraordinary capacity beyond traditional TM redox scope, which has been verified in diverse systems and attracted extensive attention.[1]

ARR schemes are universally correlated with serious setbacks including local structural transformations, voltage, and capacity degradation.[2] These hindrances originate from the complicated behavior of high-valence oxygen.[3] For ARR-related battery degradation, the coupling between high-valence oxygen and inter-layer/intra-layer cationic migration is proposed to bring about voltage hysteresis and degradation.[4] From band structure perspectives, the continuous decrease of the average TM valence state and activation of lower voltage TM redox couple is suggested to induce gradual voltage degradation.[5] Irreversible charge compensation on ligand oxygen further plays an important part, where the extreme case demonstrates O_2 release at high voltage.[6] All these procedures add up to ARR cathode fading.

During battery degradation, ARR-related surface fading has been the most intriguing but mysterious part. According to recent research, oxygen vacancies produced at the particle surface can migrate or inject towards the inside lattice, leading to bulk degradation involving nanovoid formation.[7] High-valence oxygen further necessitates its de-coordination to a single covalent bonding partner through the formation of vacancies at neighboring cation sites.[8] Such coupling drives cation disorder and manifests as layered to spinel, or rock salt phase transition,[9] which mostly occurs at the particle surface. In ARR active sodium ion cathodes, it is verified that voltage degradation actually results from surface TM valence decrease, which questions the widespread belief that ARR involves intrinsic voltage degradation.[10] On the electrolyte side, ARR behavior is verified to influence cathode electrolyte interphase (CEI) evolution,[11] released oxygen may further react with the nonaqueous electrolyte.[12] Seemingly, high-valence oxygen at the surface not only exerts a complicated effect on the inorganic bulk lattice, but is also active in CEI-related interface reactions. Nonetheless, the detailed behavior of surface high-valence oxygen has been unclear so far.

The direct probe of high-valence oxygen has been a challenging topic, particularly across cathode surface regions. The hard X-ray photoelectron spectroscopy (HAXPES) can directly characterize oxygen state evolution, the limited probe depth further makes it sensitive to surface reactions.[13] However, the high-valence oxygen related signal can only be obtained from delicate HAXPES spectra fitting where a series of surface species related features overlap and merge altogether. O-K edge X-ray absorption spectroscopy (XAS) is another widely utilized technique to probe the valence change of oxygen, but the strong TM-O hybridization feature may well overlap and mingle with that of high-valence oxygen.[14] Oxygen's participation in interface reaction can only be indirectly analyzed from the TM-O hybridization effect. The rapid development of mapping of resonant inelastic X-ray scattering (mRIXS) enables further disentangling signal of high valence oxygen from TM-O

hybridization features with extra resolving power on the emitted photon energy scale, which has been widely utilized to investigate bulk ARR behavior in past years.[10, 15] To probe surface oxygen, element-sensitive techniques with proper space resolution or bulk/surface contrast are necessary. An example is the combination of mRIXS and soft X-ray scanning transmission X-ray microscopy (STXM) to directly probe ARR and ARR-related oxygen vacancy penetration from the surface into bulk.[16] While on the whole, the direct and detailed probe of high-valence oxygen behavior across the ARR cathode surface has been deficient, and the correlation between interface high-valence oxygen and battery degradation has not been established yet.

In this work, high-valence oxygen evolution is investigated by mapping of resonant Auger electronic spectroscopy (mRAS)[17] and ambient pressure X-ray photoelectron spectroscopy (APXPS)[18] at high voltage $LiCoO_2$ surface. The high-valence oxygen signal can be well disentangled from TM-O hybridization by mRAS. Compared with the active high-valence oxygen in $LiCoO_2$ bulk, no high-valence oxygen can be probed on the $LiCoO_2$ surface. Such contrast indicates that high-valence oxygen can not sustain at the cathode surface but diminish and fade in the radial direction. By introducing O_2 in the vacuum chamber, the interface reaction between O_2 and CEI external surface can be further probed by APXPS. It is found that the CEI layer can be oxidized and deteriorated from released oxygen contact, which further influences electrochemical performances. This work verified the interface degradation mode of high-valence oxygen at high voltage. These findings indicate that stabilizing high-valence oxygen at the particle surface is the key to exploiting ARR capacity with superior cycle stability.

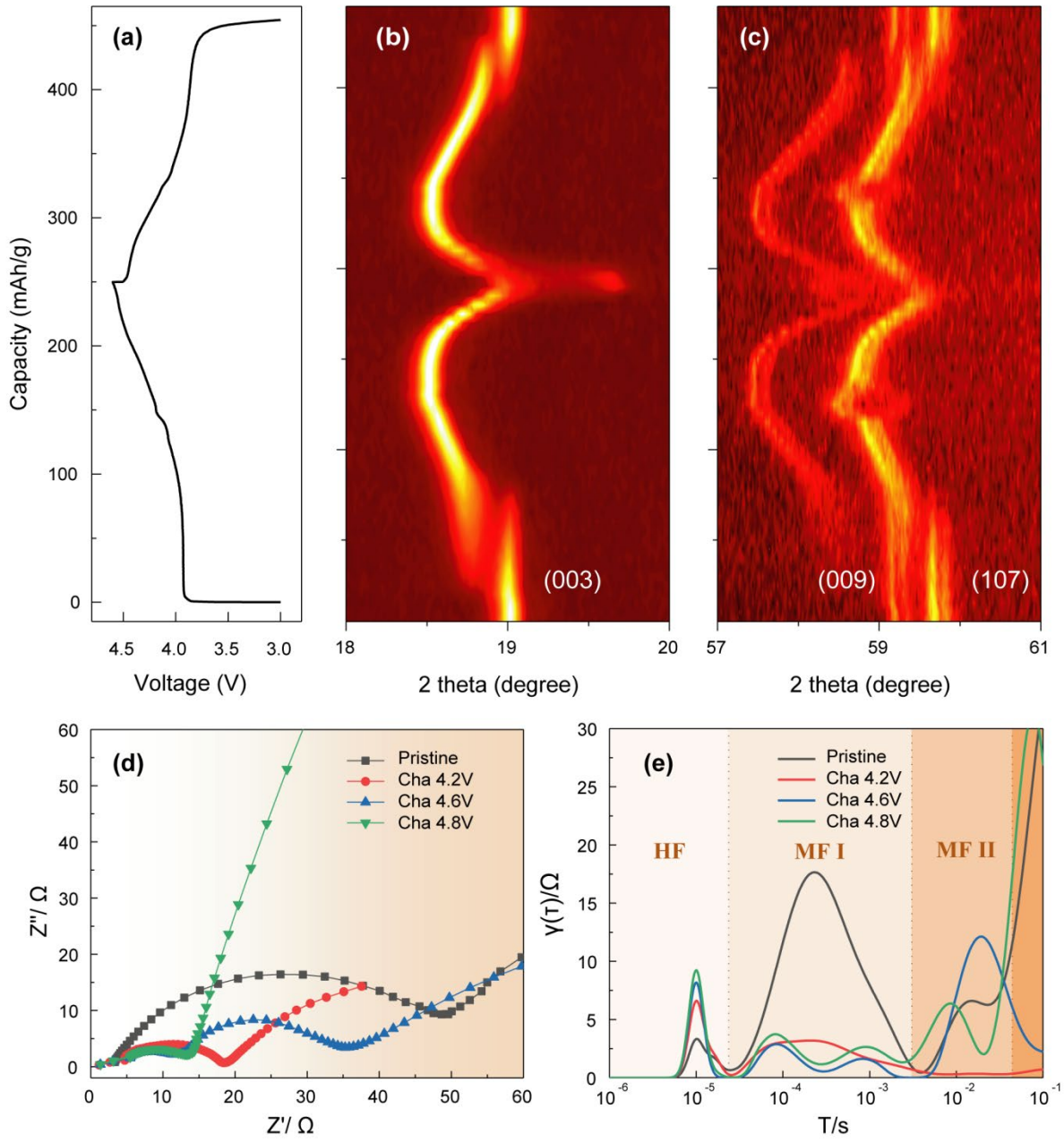

Figure 1. Electrochemical, structural and impedance characterizations of $LiCoO_2$. a. charge-discharge voltage profiles within voltage 3.0-4.6 V in the first cycle. b, c. corresponding in-situ XRD patterns of $LiCoO_2$ at different voltages. d, e. EIS and DRT analysis of $LiCoO_2$ surface in the first charge process. HF and MF indicate high frequency and middle frequency regions.

Figure 1a shows the voltage profile of standard $LiCoO_2$ in the first cycle in the voltage range of 3.0-4.6 V at 0.1C. The first charge delivers a capacity of 231 mAh/g, and the discharge retains 198 mAh/g. $LiCoO_2$ overall presents a solid solution reaction scheme, in which voltage plateau and slight voltage fluctuation can be detected at 3.9 V and 4.15 V, as can be found in the dQ/dV curve in Figure S1. These two features correspond to the first-order insulator-metal transition[19] and order-disorder transition,[20] respectively. Figure 1b and Figure 1c show in-situ XRD contour plots at a diffraction angle of 19-20° and 57-61°, which corresponds to (003) and (107) peak regions, respectively. The (003) peak shifts to a lower diffraction angle during charge and shift back upon further charge to 4.6 V, which originates from the deintercalation-induced phase transitions from O3 to H1-3 and further to O1 geometries.[21] Meanwhile, the (107) peak demonstrates splitting at 4.6 V, which results from the order-disorder phase transition from Li and vacancy intralayer arrangement.[20] Such redox behavior and structural evolution demonstrate the conventional electrochemical response of layered $LiCoO_2$ in R-3m geometry. To probe the interface response, Figure 1d shows the electrochemical impedance spectroscopy (EIS) results of $LiCoO_2$ at different charge/discharge states. Semicircles can be detected at low and high frequencies, which can be attributed to the CEI layer formation process and charge transfer process, respectively.[22] The distribution of relaxation time (DRT) analysis further deconvolutes the EIS results into different frequency regions (Figure 1e), which provide information on the Li diffusion and charge transfer characteristic features. Upon delithiation, the characteristic peak changes in HF, MF I, and MF II regions indicate the CEI layer, cathode electronic properties, and charge transfer step evolution, respectively. The dramatic EIS and DRT evolution implies serious interface reactions at high voltage.

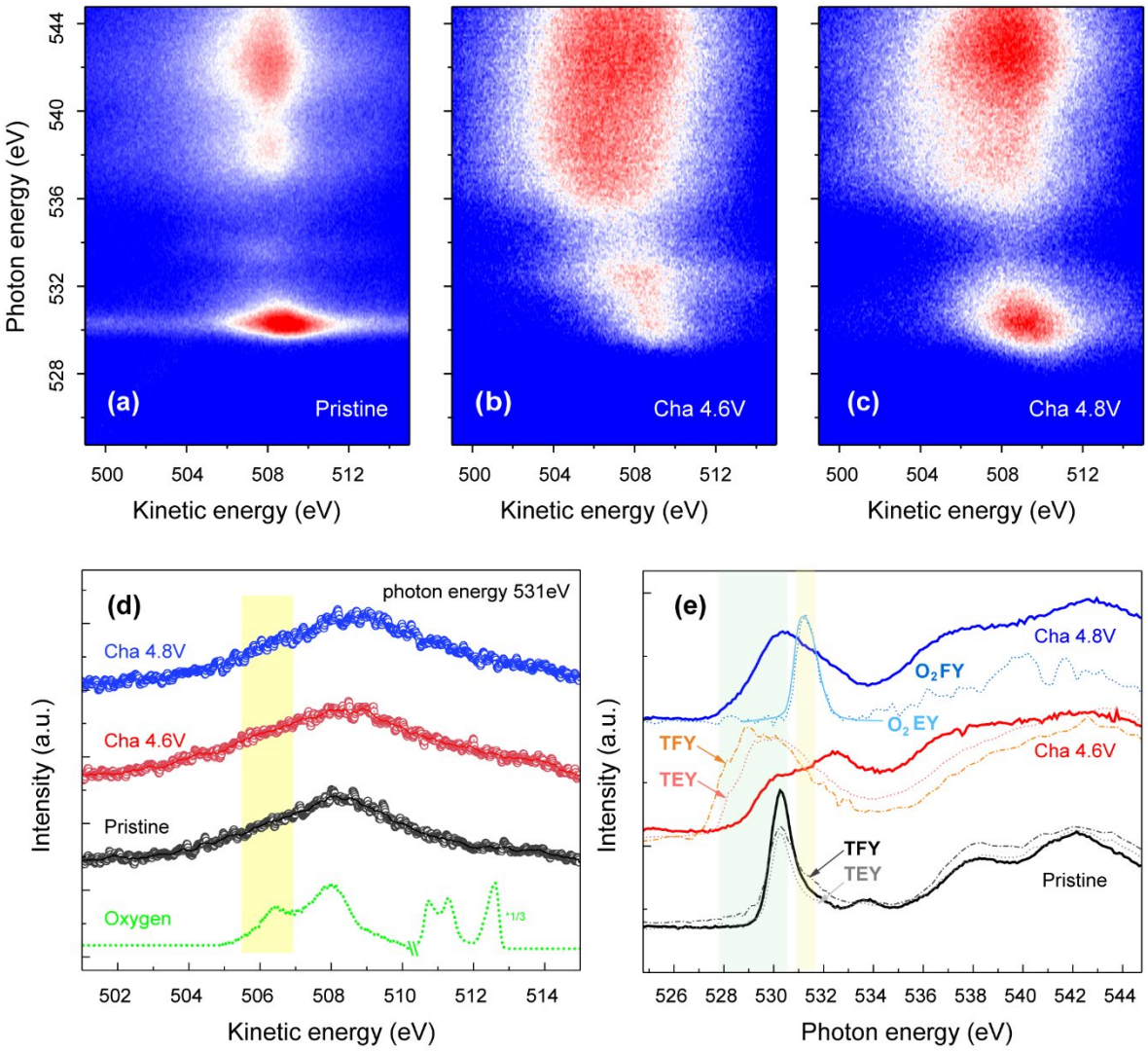

Figure 2. High-valence oxygen states probe of $LiCoO_2$ surface. a-c, color-coded mRAS of $LiCoO_2$ at pristine (a), charged 4.6 V (b), charged 4.8 V (c) states. d, mRAS cut from 531 eV at different electrochemical states (solid line). The result of pure O_2 is added for comparison. e, O-K edge XAS of $LiCoO_2$ at different electrochemical states in Auger electron yield (solid line), in comparison with corresponding XAS in total electron yield (TEY), total fluorescence yield (TFY) modes and XAS from pure O_2.

To directly probe the high-valence oxygen on $LiCoO_2$ surfaces, mRAS is carried out at different electrochemical states. The schematic diagram of the fundamental process of mRAS is shown in Figure S2, together with that of mRIXS. In a typical

mRAS characterization, the incident photon energy is scanned across the absorption edge, and the emitted Auger electrons at each resonant energy are further resolved in kinetic energy (KE). This approach provides an additional dimension of information along the KE of Auger electrons, which provides extra sensitivity to the electronic states near the absorption edge.[17] Considering the limited escape depth of emitted electrons, mRAS is surface sensitive with probe depth around several nanometers. The high sensitivity and the shallow probe depth make mRAS a proper choice to capture surface high-valence oxygen signals.

Figure 2a-c shows the mRAS result of $LiCoO_2$ at pristine, charged 4.6 V and charged 4.8 V states, respectively. The incident energy is scanned in 525-545 eV, while the KE is resolved in 499-515 eV. Overall, the mRAS feature at incident energy ~530 eV, KE~508 eV can be attributed to the hybridization from Co 3d and O 2p states, and the mRAS feature at incident energy above 537 eV, KE~508 eV originates from hybridization between Co 4sp and O 2p states. Upon delithiation, the Co 3d-O 2p hybridization features evolve to lower incident energy region, and slight carbonate features appear at incident energy ~534 eV. These changes can be attributed to Co oxidization and carbonate species formation on the cathode surface,[14b, 23] which is further supported by XAS below.

In previous research, different viewpoints have been proposed on the fundamental properties of high valence oxygen. Recent progress indicates that trapped oxygen molecules in crystal lattice are actually the physics origin of oxidized oxygen and ARR capacity.[24] It is then necessary to compare the mRAS of charged electrode and oxygen molecules to fingerprint surface oxygen behavior. In past years, mRIXS has been extensively utilized to directly probe oxidized oxygen in diverse ARR cathodes and obtained much progress.[1a, 1b, 25] The fundamental origin of the oxidized oxygen feature is still not clear yet and is not the focus of this work. However, high-valence oxygen features are overall consistent in various ARR cathodes, which also agree with that of O_2.[16b, 26] Such consistency indicates that oxidized oxygen and oxygen molecule share analogous and consistent electronic states. Note that mRIXS and mRAS share identical excitation process, but collect parallel de-excitation channels (photon vs electron). The direct comparison between electrodes at different state of charge and O_2 in both mRAS and mRIXS can consequently provide valuable and unique information on ARR behavior at the cathode surface.

From conventional O-K edge XAS, high-valence oxygen demonstrates shoulder peak at incident energy 531 eV in both electron and fluorescence yields. Previous works on mRIXS characterization further indicate that high-valence oxygen evolves at incident energy ~531 eV and emitted photon energy ~523 eV.[1d, 26c] Such a high-valence oxygen feature can be well disentangled from TM-O hybridization along the emission photon energy scale, Figure S3. To fingerprint the high-valence oxygen at the cathode surface, resonant Auger spectra (RAS), ie mRAS cut at 531 eV at different charge states are plotted together with O_2 results in Figure 2d. With extra sensitivity along the kinetic energy scale, O_2 demonstrates three sharp energy loss features at kinetic energy 512.6 eV, 511.3 eV, 510.7 eV and two evident de-excitation features at kinetic energy 508.0 eV, 506.4 eV, respectively, which is quite distinguished from that of charged $LiCoO_2$. The overall broad RAS feature of delithiated $LiCoO_2$ at kinetic energy 508.5 eV comes from the Auger de-excitation from conventional TM-O hybridized valence band. In parallel RIXS results in Figure S3, a sharp feature from oxidized oxygen at 523.3 eV rises against the broad valence band feature at 524.8 eV. Oxidized oxygen agrees well with oxygen molecule features in mRIXS, while no features associated with high-valence oxygen can be detected in mRAS. It is worth mentioning that despite the parallel de-excitation channel, energy offset occurs between kinetic energy in mRAS and emitted photon energy in mRIXS. The spectra difference can be attributed to the screening effect when electrons escape cathode surfaces into the vacuum, overcoming the work function and other related effects, Figure S3. In brief, it is obvious that the high-valence oxygen in bulk $LiCoO_2$ (mRIXS)[25, 26c] does not occur at the $LiCoO_2$ surface (mRAS), such contrast indicates that the intrinsic high-valence oxygen deteriorates on the cathode particle surface.

One may argue that CEI species formation may cover the interface of $LiCoO_2$ active material, where high-valence oxygen would occur. Figure 2e compares the O-K edge sXAS of $LiCoO_2$ at different states in Auger electron yield (AEY) mode, accompanied by corresponding XAS in TEY/TFY. O-K edge sXAS of O_2 integrated from RIXS as in fluorescence yield (FY) and from mRAS as in electron yield (EY) mode are added for comparison. The O-K edge XAS evolution well supports the Co oxidization and carbonated species formation upon charge.[14b, 23] Note that these features are excited at different threshold energies, where TM-O hybridization mostly at 528~530 eV, surface carbonate species at ~534 eV, while oxidized oxygen at ~531 eV. As a result, at resonant energy 531 eV the oxidized oxygen signal can be selectively excited and dominate the final yield, which demonstrates the unique advantage of mRAS. Most importantly, despite the shallow probe depth of AEY mode, the signal from TM-O hybridization can be well probed, indicating that the AEY or mRAS may well penetrate the outmost CEI layer and collect signal from $LiCoO_2$ active material region. These results validate that on $LiCoO_2$ cathode, high-valence oxygen does deteriorate at the active particle surface. Seemingly, the surface structural change and TM valence change from surface to bulk are accompanied by the valence change of oxygen,[9a, 16a] where the valence of oxygen decreases from bulk to surface in the radial direction. Actually, such contrast agrees well with our previous claim that high-valence oxygen needs to be stabilized at the particle surface via surface doping and surface oxygen protection strategies, which is key to supporting intrinsic ARR exploitation.[26c]

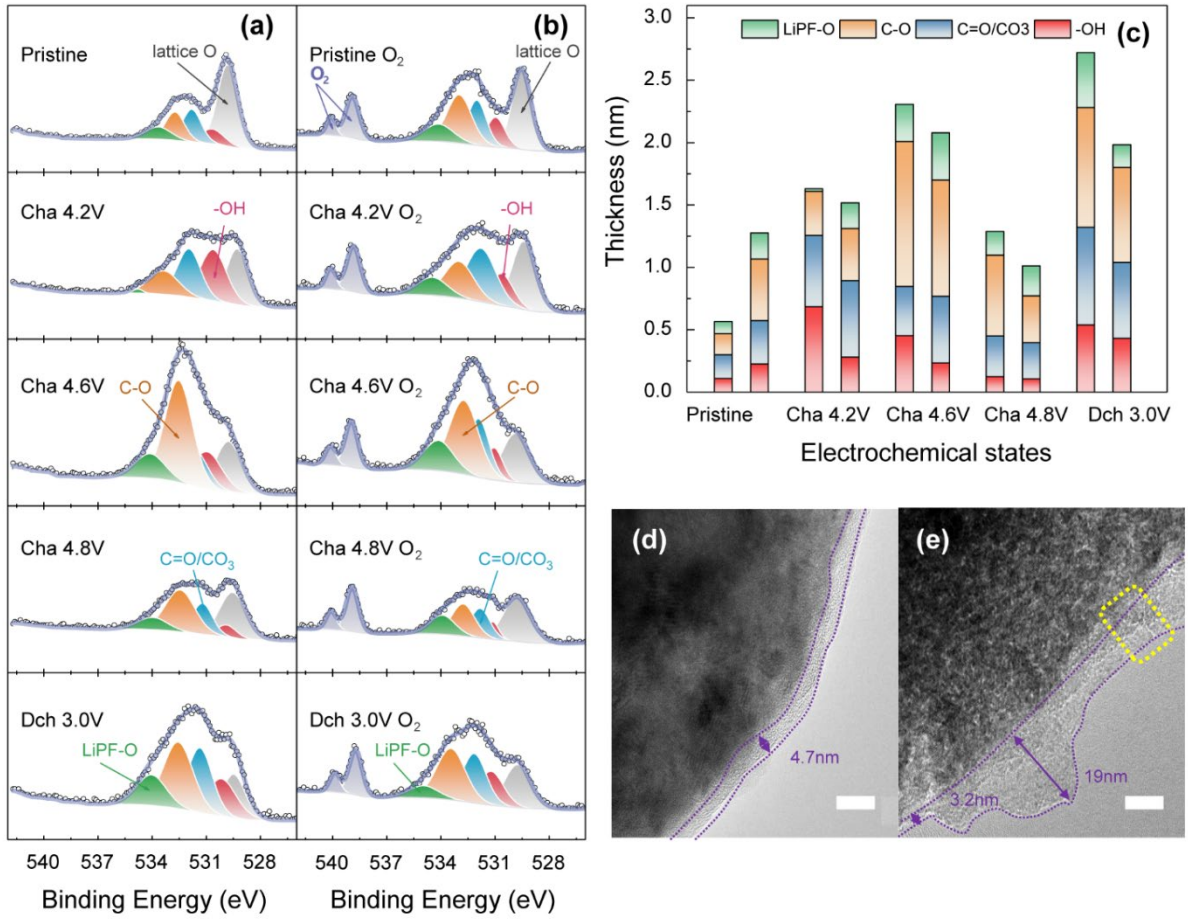

Figure 3. Interface reactions between released O_2 and $LiCoO_2$ cathode. a-b, APXPS of $LiCoO_2$ at different states from top to bottom as pristine, charged 4.2 V, charged 4.6 V, charged 4.8 V, discharged 3.0 V in vacuum (a) and 0.6 torr oxygen (b) atmosphere. c, quantified APXPS and calculated CEI species thickness at different electrochemical states in vacuum (left column) and in O_2 (right column) atmosphere, species are color-coded. Cathode particle morphology of charged 4.6 V state before (d) and after (e) O_2 contact. The scale bar is 10 nm.

High-valence oxygen degradation at the surface accompanies transition metal migration, bulk phase transition, and finally oxygen release.[6] Considering the high reactivity of released oxygen,[12] it may well participate in the interface reaction against nonaqueous electrolytes.[27] To figure out potential interface reactions, APXPS is carried out here with an oxygen inlet into the vacuum chamber. With the dedicated pressure differential system, APXPS enables in-situ and operando spectra collection at gas-solid and liquid-solid interfaces.[18, 28]

Figure 3a shows the APXPS probed at vacuum from top to bottom at pristine, charged 4.2 V, charged 4.6 V, charged 4.8 V, discharged 3.0 V states, and Figure 3b shows corresponding results at 0.6 torr O_2 atmosphere. This selected O_2 pressure is based on the accumulated oxygen partial pressure obtained from differential electrochemical mass spectroscopy (DEMS) characterization, Figure S4. The typical APXPS results can be well-fitted with five sub peaks as listed in Table S1. At high voltage, peaks from CEI components increase remarkably, overwhelming that of lattice oxygen. At charged 4.6 V, dramatic C-O species occur, such behavior coincides with the onset of O_2 release of $LiCoO_2$ probed by DEMS.[27, 29] In Figure 3b, strong peaks from inlet oxygen can be detected, verifying the surrounding oxygen atmosphere or oxygen molecule attachment on the cathode surface. Upon oxygen contact, APXPS spectra landscape and weight ratio demonstrate obvious evolution from oxidization. The spectra contrast clearly indicates that the CEI layer can be further oxidized by oxygen gas.

The quantified CEI thickness and each chemical species amount are shown in Figure 3c,[30] with a detailed quantification process in Supporting and fitting parameters in Table S2. The CEI thickness mostly decreases upon oxygen inlet, indicating the oxidization from inlet O_2. The C-O species decrease meanwhile $C=O/CO_3$ species sustain or even increase at 4.6 V and 4.8 V high voltage, indicating the oxidization of CEI components upon released O_2. Such oxidization effect can be further verified from TEM results in Figure 3d and 3e, in which the 4.6 V charged $LiCoO_2$ is characterized before and after oxygen contact for 24 h. The smooth CEI surface with a typical thickness of ~ 4.7 nm of 4.6 V $LiCoO_2$ gets further oxidized after oxygen contact and presents rough features with thickness ranging from 3.2-19 nm, where the crack formation can even be found after oxygen contact, as shown in Figure 3e.

Note that oxygen contact here can only mimic the interface reaction of the CEI external surface, oxygen itself may well participate in CEI formation from the very beginning or even presents dynamic evolution upon cycle.[11, 22] Based on some previous research, the released oxygen is actually singlet oxygen, which is chemically much more active to arouse interface

reactions.[31] Still, the CEI surface can be further oxidized upon O_2 contact experimentally, indicating incomplete CEI oxidization from lattice oxygen release. In conventional DEMS, oxygen release can only be detected in the very first cycle,[6b] such interface reaction of oxygen participation in CEI formation and evolution may well explain this phenomenon. The released lattice oxygen may well be "absorbed" in subsequent CEI evolution reactions. In brief, CEI thickness and composition change together with its morphology change all indicate the oxidization effect of the released oxygen on the CEI interface layer.

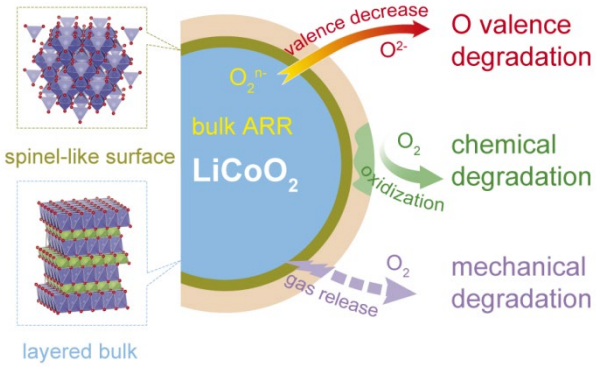

Figure 4. Schematic diagram showing the high-valence oxygen degradation process across $LiCoO_2$ cathode interface, as probed from mRAS and APXPS.

Based on the above results, the high-valence oxygen degradation mode across the interface can be illustrated in Figure 4. As can be directly verified from mRAS, high-valence oxygen can not sustain on the $LiCoO_2$ surface at high voltage. From the active particle bulk to the surface, the oxygen valence decreases in the radial direction. Oxygen participation in CEI formation and oxygen release from lattice can be parallel paths to accomplish valence degradation. Subsequently, released oxygen may further exert a destructive effect on CEI components, which can be directly detected from APXPS. Upon inlet oxygen, the CEI composition can be oxidized, CEI thickness decreases, and even CEI morphology will deteriorate. Such interface side reactions may well affect the electrochemical performances. As shown in Figure S5, after oxygen contact for 24 h, re-assembled battery degradation can be well accelerated as compared with argon contact. The distinguished battery degradation speed demonstrates the O_2-induced CEI destruction for subsequent cycles. Moreover, it should be stressed that lattice oxygen is the original source of released oxygen, as verified by isotope labeling DEMS experiment.[6a] As a result, lattice oxygen escape from the cathode framework actually starts from the bottom CEI layer instead of the outmost CEI layer. Mechanical cracking effect on the outmost layer (Figure 3e) may well occur on the inner CEI-cathode contact region. Further mechanical "pealing off" effects from oxygen release can be expected. Considering such mechanical deterioration, the destruction of released oxygen on interface reaction can be even more dramatic.

These findings present the overall degradation scheme of high-valence oxygen at the cathode surface. Even though this work is conducted on a model $LiCoO_2$ system, high-valence oxygen involving surface destruction may exist in various ARR cathode systems. The above three degradation modes will add up to surface destruction on ARR active cathodes. Such an oxygen degradation scenario can be further correlated with other surface behaviors including TM valence degradation, TM site migration, oxygen vacancy formation, and injection.[9, 16] The oxygen valence degradation and oxygen-involved CEI reaction imply that the cathode surface must be modified and stabilized before ARR capacity can be fully exploited. In previous reports, various surface modification strategies have been developed, including spinel layer coating, surface oxygen vacancy design, strengthened TM-O bond, building up isolating layer against electrolyte, oxygen predator, etc.[32] These strategies prove effective in mitigating ARR instability and improving electrochemical performances. The prevention of continuous oxygen loss and mitigation of surface CEI instability is proven prerequisites for the practical development of ARR. Yet, the original driving force and bottleneck of high-valence oxygen instability across the surface is still vague. More fundamental investigations are needed to uncover the detailed surface degradation process and realize the rational design of ARR cathode with superior performances.

In this work, high-valence oxygen degradation across the $LiCoO_2$ interface is investigated by combining mRAS and APXPS. It is verified from mRAS that high-valence oxygen in $LiCoO_2$ bulk can not sustain at the particle surface. An overall oxygen valence decrease in the radial direction can be verified from bulk to surface. Such oxygen deterioration can be correlated with oxygen gas release at high voltage. As verified from APXPS, released O_2 contact further exerts a destructive influence on the CEI layer, which leads to CEI species oxidation, thickness decrease, morphology change, and finally accelerates battery degradation. Based on these findings, a general oxygen degradation scheme including valence degradation, chemical degradation, and mechanical degradation can be established here on the $LiCoO_2$ model system. Such an effect of high-valence oxygen instability on the cathode surface may well occur in other high-energy density cathodes utilizing ARR. Figuring out the driving force of surface degradation and stabilizing surface oxygen is proven a prerequisite to the practical development of ARR-based cathodes.

Acknowledgements

This work is supported by CAS Project for Young Scientists in Basic Research (Grant No. YSBR-058), National Science Foundation of China (No. 22179066, No. 21902179), Shandong Provincial Natural Science Foundation (ZR202103010205), and the Startup Foundation for Advanced Talents in Qingdao University (DC2000005106). The authors thank the BL02B of SSRF supported by NSFC No. 11227902. This research uses resources of the Advanced Light Source, which is a DOE Office of Science User Facility under contract No. DE-AC02-05CH11231.

Keywords: Lithium-ion batteries • Anionic redox reaction • Cathode electrolyte interphase • X-ray spectroscopy

Reference

[1] a) W. Zuo, M. Luo, X. Liu, J. Wu, H. Liu, J. Li, M. Winter, R. Fu, W. Yang, Y. Yang, *Energy Environ Sci* **2020**, *13*, 4450-4497; b) G.-H. Lee, V. W.-h. Lau, W. Yang, Y.-M. Kang,

Adv. Energy Mater. **2021**, *11*, 2003227; c) S. Zhao, K. Yan, J. Zhang, B. Sun, G. Wang, *Angew. Chem. Int. Ed.* **2021**, *60*, 2208-2220; d) G.-H. Lee, J. Wu, D. Kim, K. Cho, M. Cho, W. Yang, Y.-M. Kang, *Angew. Chem. Int. Ed.* **2020**, *59*, 8681-8688.

[2] G. Assat, J.-M. Tarascon, *Nat Energy* **2018**, *3*, 373-386.

[3] a) M. Ben Yahia, J. Vergnet, M. Saubanere, M.-L. Doublet, *Nat. Mater.* **2019**, *18*, 496-502; b) D.-H. Seo, J. Lee, A. Urban, R. Malik, S. Kang, G. Ceder, *Nat Chem* **2016**, *8*, 692-697.

[4] Q. Wang, S. Mariyappan, G. Rousse, A. V. Morozov, B. Porcheron, R. Dedryvère, J. Wu, W. Yang, L. Zhang, M. Chakir, M. Avdeev, M. Deschamps, Y.-S. Yu, J. Cabana, M.-L. Doublet, A. M. Abakumov, J.-M. Tarascon, *Nat. Mater.* **2021**, *20*, 353-361.

[5] E. Hu, X. Yu, R. Lin, X. Bi, J. Lu, S. Bak, K.-W. Nam, H. L. Xin, C. Jaye, D. A. Fischer, K. Amine, X.-Q. Yang, *Nat Energy* **2018**, *3*, 690-698.

[6] a) K. Luo, M. R. Roberts, R. Hao, N. Guerrini, D. M. Pickup, Y.-S. Liu, K. Edström, J. Guo, A. V. Chadwick, L. C. Duda, P. G. Bruce, *Nat Chem* **2016**, *8*, 684-691; b) E. Castel, E. J. Berg, M. El Kazzi, P. Novák, C. Villevieille, *Chem. Mater.* **2014**, *26*, 5051-5057.

[7] P. Yan, J. Zheng, Z.-K. Tang, A. Devaraj, G. Chen, K. Amine, J.-G. Zhang, L.-M. Liu, C. Wang, *Nat. Nanotechnol.* **2019**, *14*, 602-608.

[8] J. Hong, W. E. Gent, P. Xiao, K. Lim, D.-H. Seo, J. Wu, P. M. Csernica, C. J. Takacs, D. Nordlund, C.-J. Sun, K. H. Stone, D. Passarello, W. Yang, D. Prendergast, G. Ceder, M. F. Toney, W. C. Chueh, *Nat. Mater.* **2019**, *18*, 256-265.

[9] a) M. Gu, I. Belharouak, J. Zheng, H. Wu, J. Xiao, A. Genc, K. Amine, S. Thevuthasan, D. R. Baer, J.-G. Zhang, N. D. Browning, J. Liu, C. Wang, *ACS Nano* **2013**, *7*, 760-767; b) J. Qiu, X. Liu, R. Chen, Q. Li, Y. Wang, P. Chen, L. Gan, S.-J. Lee, D. Nordlund, Y. Liu, X. Yu, X. Bai, H. Li, L. Chen, *Adv. Funct. Mater.* **2020**, *30*, 1909392.

[10] J. Wu, Z. Zhuo, X. Rong, K. Dai, Z. Lebens-Higgins, S. Sallis, F. Pan, L. F. J. Piper, G. Liu, Y.-d. Chuang, Z. Hussain, Q. Li, R. Zeng, Z.-x. Shen, W. Yang, *Sci Adv* **2020**, *6*, eaaw3871.

[11] Q. Li, Y. Wang, X. Wang, X. Sun, J.-N. Zhang, X. Yu, H. Li, *ACS Appl Mater Inter* **2020**, *12*, 2319-2326.

[12] a) L. A. Kaufman, B. D. McCloskey, *Chem. Mater.* **2021**, *33*, 4170-4176; b) A. T. S. Freiberg, M. K. Roos, J. Wandt, R. de Vivie-Riedle, H. A. Gasteiger, *J. Phys. Chem. A* **2018**, *122*, 8828-8839.

[13] a) G. Assat, D. Foix, C. Delacourt, A. Iadecola, R. Dedryvère, J. M. Tarascon, *Nat Commun* **2017**, *8*, 1-12; b) G. Assat, A. Iadecola, D. Foix, R. Dedryvere, J.-M. Tarascon, *ACS Energy Lett* **2018**, *3*, 2721-2728.

[14] a) W. Yang, T. P. Devereaux, *J. Power Sources* **2018**, *389*, 188-197; b) S. Roychoudhury, R. Qiao, Z. Zhuo, Q. Li, Y. Lyu, J.-H. Kim, J. Liu, E. Lee, B. J. Polzin, J. Guo, S. Yan, Y. Hu, H. Li, D. Prendergast, W. Yang, *Energy Environ Mater* **2021**, *4*, 246-254.

[15] a) D. Eum, B. Kim, S. J. Kim, H. Park, J. Wu, S.-P. Cho, G. Yoon, M. H. Lee, S.-K. Jung, W. Yang, W. M. Seong, K. Ku, O. Tamwattana, S. K. Park, I. Hwang, K. Kang, *Nat. Mater.* **2020**, *19*, 419-427; b) Z. Zhuo, K. Dai, J. Wu, L. Zhang, N. Tamura, Y.-d. Chuang, J. Feng, J. Guo, Z.-x. Shen, G. Liu, F. Pan, W. Yang, *ACS Energy Lett* **2021**, 3417-3424.

[16] a) P. M. Csernica, S. S. Kalirai, W. E. Gent, K. Lim, Y.-S. Yu, Y. Liu, S.-J. Ahn, E. Kaeli, X. Xu, K. H. Stone, A. F. Marshall, R. Sinclair, D. A. Shapiro, M. F. Toney, W. C. Chueh, *Nat Energy* **2021**, *6*, 642-652; b) W. E. Gent, K. Lim, Y. Liang, Q. Li, T. Barnes, S.-J. Ahn, K. H. Stone, M. McIntire, J. Hong, J. H. Song, Y. Li, A. Mehta, S. Ermon, T. Tyliszczak, D. Kilcoyne, D. Vine, J.-H. Park, S.-K. Doo, M. F. Toney, W. Yang, D. Prendergast, W. C. Chueh, *Nat Commun* **2017**, *8*, 2091.

[17] H. Zhang, X. Li, W. Wang, B. Mao, Y. Han, Y. Yu, Z. Liu, *Rev. Sci. Instrum.* **2020**, *91*, 123108.

[18] J. Cai, Q. Dong, Y. Han, B.-H. Mao, H. Zhang, P. G. Karlsson, J. Åhlund, R.-Z. Tai, Y. Yu, Z. Liu, *Nucl Sci Tech* **2019**, *30*, 81.

[19] a) C. A. Marianetti, G. Kotliar, G. Ceder, *Nat Mater* **2004**, *3*, 627-631; b) M. Menetrier, I. Saadoune, S. Levasseur, C. Delmas, *J. Mater. Chem.* **1999**, *9*, 1135-1140.

[20] a) J. N. Reimers, J. R. Dahn, *J. Electrochem. Soc.* **1992**, *139*, 2091-2097; b) Y. Shao-Horn, S. Levasseur, F. Weill, C. Delmas, *J. Electrochem. Soc.* **2003**, *150*, A366-A373.

[21] A. Van der Ven, M. K. Aydinol, G. Ceder, G. Kresse, J. Hafner, *Phys. Rev. B* **1998**, *58*, 2975-2987.

[22] J.-N. Zhang, Q. Li, Y. Wang, J. Zheng, X. Yu, H. Li, *Energy Storage Mater* **2018**, *14*, 1-7.

[23] a) T. Mizokawa, Y. Wakisaka, T. Sudayama, C. Iwai, K. Miyoshi, J. Takeuchi, H. Wadati, D. G. Hawthorn, T. Z. Regier, G. A. Sawatzky, *Phys. Rev. Lett.* **2013**, *111*, 056404; b) Z. Zhuo, P. Lu, C. Delacourt, R. Qiao, K. Xu, F. Pan, S. J. Harris, W. Yang, *Chem. Commun.* **2018**, *54*, 814-817.

[24] a) R. A. House, G. J. Rees, M. A. Pérez-Osorio, J.-J. Marie, E. Boivin, A. W. Robertson, A. Nag, M. Garcia-Fernandez, K.-J. Zhou, P. G. Bruce, *Nat Energy* **2020**, *5*, 777-785; b) R. A. House, J.-J. Marie, J. Park, G. J. Rees, S. Agrestini, A. Nag, M. Garcia-Fernandez, K.-J. Zhou, P. G. Bruce, *Nat Commun* **2021**, *12*, 2975.

[25] E. Hu, Q. Li, X. Wang, F. Meng, J. Liu, J.-N. Zhang, K. Page, W. Xu, L. Gu, R. Xiao, H. Li, X. Huang, L. Chen, W. Yang, X. Yu, X.-Q. Yang, *Joule* **2021**, *5*, 720-736.

[26] a) Z. Zhuo, C. D. Pemmaraju, J. Vinson, C. Jia, B. Moritz, I. Lee, S. Sallies, Q. Li, J. Wu, K. Dai, Y.-d. Chuang, Z. Hussain, F. Pan, T. P. Devereaux, W. Yang, *J Phys Chem Lett* **2018**, *9*, 6378-6384; b) Z. Zhuo, Y.-s. Liu, J. Guo, Y.-d. Chuang, F. Pan, W. Yang, *J Phys Chem Lett* **2020**, *11*, 2618-2623; c) J.-N. Zhang, Q. Li, C. Ouyang, X. Yu, M. Ge, X. Huang, E. Hu, C. Ma, S. Li, R. Xiao, W. Yang, Y. Chu, Y. Liu, H. Yu, X.-Q. Yang, X. Huang, L. Chen, H. Li, *Nat Energy* **2019**, *4*, 594-603.

[27] J. K. Papp, N. Li, L. A. Kaufman, A. J. Naylor, R. Younesi, W. Tong, B. D. McCloskey, *Electrochim. Acta* **2021**, *368*, 137505.

[28] Y. Han, H. Zhang, Y. Yu, Z. Liu, *ACS Catalysis* **2021**, *11*, 1464-1484.

[29] H. Wang, E. Rus, T. Sakuraba, J. Kikuchi, Y. Kiya, H. D. Abruña, *Anal. Chem.* **2014**, *86*, 6197-6201.

[30] a) N. Schulz, R. Hausbrand, L. Dimesso, W. Jaegermann, *J. Electrochem. Soc.* **2018**, *165*, A819-A832; b) N. Philip, W. Martin, *Langmuir* **2013**, *29*, 15813-15821.

[31] B. L. D. Rinkel, J. P. Vivek, N. Garcia-Araez, C. P. Grey, *Energy Environ Sci* **2022**, *15*, 3416-3438.

[32] a) X.-D. Zhang, J.-L. Shi, J.-Y. Liang, Y.-X. Yin, J.-N. Zhang,

X.-Q. Yu, Y.-G. Guo, *Adv. Mater.* **2018**, *30*, 1801751; b) Y. Zhao, J. Liu, S. Wang, R. Ji, Q. Xia, Z. Ding, W. Wei, Y. Liu, P. Wang, D. G. Ivey, *Adv. Funct. Mater.* **2016**, *26*, 4760-4767; c) Q. Shao, P. Gao, C. Yan, M. Gao, W. Du, J. Chen, Y. Yang, J. Gan, Z. Wu, C. Zhang, G. Chen, X. Zheng, Y. Lin, Y. Jiang, W. Sun, Y. Liu, M. Gao, H. Pan, *Adv. Mater.* **2022**, *34*, 2108543; d) D. Luo, J. Cui, B. Zhang, J. Fan, P. Liu, X. Ding, H. Xie, Z. Zhang, J. Guo, F. Pan, Z. Lin, *Adv. Funct. Mater.* **2021**, *31*, 2009310; e) Q. Li, D. Zhou, L. Zhang, D. Ning, Z. Chen, Z. Xu, R. Gao, X. Liu, D. Xie, G. Schumacher, X. Liu, *Adv. Funct. Mater.* **2019**, *29*, 1806706; f) Z. Li, Y. Li, M. Zhang, Z.-W. Yin, L. Yin, S. Xu, C. Zuo, R. Qi, H. Xue, J. Hu, B. Cao, M. Chu, W. Zhao, Y. Ren, L. Xie, G. Ren, F. Pan, *Adv. Energy Mater.* **2021**, *11*, 2101962; g) Q. Ma, Z. Chen, S. Zhong, J. Meng, F. Lai, Z. Li, C. Cheng, L. Zhang, T. Liu, *Nano Energy* **2021**, *81*, 105622; h) Q. Li, D. Ning, D. Zhou, K. An, D. Wong, L. Zhang, Z. Chen, G. Schuck, C. Schulz, Z. Xu, G. Schumacher, X. Liu, *J. Mater. Chem. A* **2020**, *8*, 7733-7745; i) S. Y. Kim, C. S. Park, S. Hosseini, J. Lampert, Y. J. Kim, L. F. Nazar, *Adv. Energy Mater.* **2021**, *11*, 2100552.

Entry for the Table of Contents

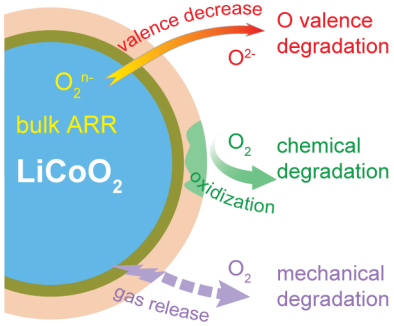

By combining synchrotron-based mRAS and APXPS, an integrated high-valence oxygen degradation scenario is established at the cathode surface. Compared with mRIXS, mRAS verified oxygen valence decrease from bulk to surface. APXPS further proves the CEI layer oxidized and deteriorated by O_2. The high-valence oxygen degradation involving valence, chemical, and mechanical change can be general surface fading behavior in ARR active cathodes.